Draft version June 18, 2009
Preprint typeset using LaTeX style emulateapj v. 03/07/07

THE HST/ACS COMA CLUSTER SURVEY: II - DATA DESCRIPTION AND SOURCE CATALOG[1]

Derek Hammer[2,13], Gijs Verdoes Kleijn[3], Henry C. Ferguson[4], Paul Goudfrooij[4], Marc Balcells[5], Carlos Hoyos[6], Mark den Brok[3], David Carter[7], Rafael Guzmán[6], Reynier F. Peletier[3], Alfonso L. Aguerri[5], Dan Batcheldor[8], Terry J. Bridges[9], Jonathan I. Davies[10], Peter Erwin[11], Alister W. Graham[12], Ann Hornschemeier[13], Michael J. Hudson[14], Avon Huxor[15], Shardha Jogee[16], Yutaka Komiyama[17], Jennifer Lotz[18], John R. Lucey[19], Ronald O. Marzke[20], David Merritt[8], Bryan W. Miller[21], Neal A. Miller[22,23,2], Bahram Mobasher[24], Mustapha Mouhcine[7], Sadanori Okamura[25], Steven Phillipps[15], Bianca M. Poggianti[26], Thomas H. Puzia[27], Ray M. Sharples[19], Russell J. Smith[19], Neil Trentham[28], R. Brent Tully[29], Edwin Valentijn[3]

Draft version June 18, 2009

ABSTRACT

The Coma cluster, Abell 1656, is the target of a HST ACS Treasury program designed for deep imaging in the F475W and F814W passbands, covering a total area of 740 arcmin^2 (0.63 Mpc^2) over a wide range of cluster-centric radii. The survey was just 28% complete when the program was interrupted by the failure of the ACS instrument on January 27 2007, with the majority of observed fields located near the core region of Coma (19/25 pointings). In this paper we present properties of the source catalog generated from the available data, including a detailed description of the data reduction methodology used for object detection and photometry, the subtraction of bright galaxies to measure faint neighboring objects, and simulations to assess the photometric accuracy and completeness of the catalog. The final catalog consist of xxx sources. We report photometric flux limits of $g_{475} = xx$ and $i_{814} = xx$.

Subject headings: galaxies: clusters – instrument: HST: ACS

1. INTRODUCTION

The Coma cluster has been the subject of numerous surveys from X-ray to radio owing to its richness, proximity ($z \sim 0.023$), and location at high Galactic latitude ($b \sim 0.88°$). Coma members have supplied information critical to our understanding of galaxy formation and evolution in dense environments, and provide a local benchmark for studies of galaxy evolution in different environments and at higher redshift. However, the properties of intrinsically faint objects are not well characterized in the Coma cluster compared to other well-studied local clusters such as Virgo and Fornax. The resolution and sensitivity afforded by the *Hubble Space Telescope-Advanced Camera for Surveys* (HST-ACS; Ford et al. 1998) allows for a detailed analysis of faint and compact systems in Coma, such as constraining the globular cluster population, measuring the structural parameters of dwarf galaxies, and identifying the nature of com-

[1] Based on observations with the NASA/ESA *Hubble Space Telescope* obtained at the Space Telescope Science Institute, which is operated by the association of Universities for Research in Astronomy, Inc., under NASA contract NAS 5-26555. These observations are associated with program GO10861.

[2] Department of Physics and Astronomy, Johns Hopkins University, 3400 North Charles Street, Baltimore, MD 21218, USA.
[3] Kapteyn Astronomical Institute, University of Groningen, PO Box 800, 9700 AV Groningen, The Netherlands.
[4] Space Telescope Science Institute, 3700 San Martin Drive, Baltimore, MD 21218, USA.
[5] Instituto de Astrofísica de Canarias, C/Vía Lactea s/n, 38200 La Laguna, Tenerife, Spain.
[6] Department of Astronomy, University of Florida, PO Box 112055, Gainesville, FL 32611, USA.
[7] Astrophysics Research Institute, Liverpool John Moores University, Twelve Quays House, Egerton Wharf, Birkenhead CH41 1LD, UK.
[8] Department of Physics, Rochester Institute of Technology, 85 Lomb Memorial Drive, Rochester, NY 14623, USA.
[9] Department of Physics, Engineering Physics and Astronomy, Queen's University, Kingston, Ontario K7L 3N6, Canada.
[10] School of Physics and Astronomy, Cardiff University, The Parade, Cardiff CF24 3YB, UK.
[11] Max-Planck-Institut für Extraterrestrische Physik, Giessenbachstrasse, D-85748 Garching, Germany.
[12] Centre for Astrophysics and Supercomputing, Swinburne University of Technology, Hawthorn, VIC 3122, Australia.
[13] Laboratory for X-Ray Astrophysics, NASA Goddard Space Flight Center, Code 662.0, Greenbelt, MD 20771, USA.
[14] Department of Physics and Astronomy, University of Waterloo, 200 University Avenue West, Waterloo, Ontario N2L 3G1, Canada.
[15] Astrophysics Group, H. H. Wills Physics Laboratory, University of Bristol, Tyndall Avenue, Bristol BS8 1TL, UK.
[16] Department of Astronomy, University of Texas at Austin, 1 University Station C1400, Austin, TX 78712, USA.
[17] Subaru Telescope, National Astronomical Observatory of Japan, 650 North A'ohoku Place, Hilo, HI 96720, USA.
[18] Leo Goldberg Fellow, National Optical Astronomy Observatory, 950 North Cherry Avenue, Tucson, AZ 85719, USA.
[19] Department of Physics, University of Durham, South Road, Durham DH1 3LE, UK.
[20] Department of Physics and Astronomy, San Francisco State University, San Francisco, CA 94132-4163, USA.
[21] Gemini Observatory, Casilla 603, La Serena, Chile.
[22] Department of Astronomy, University of Maryland, College Park, MD, 20742-2421, USA
[23] Jansky Fellow of the National Radio Astronomy Observatory. The National Radio Astronomy Observatory is a facility of the National Science Foundation operated under cooperative agreement by Associated Universities, Inc.
[24] Department of Physics and Astronomy, University of California, Riverside, CA, 92521, USA
[25] Department of Astronomy, University of Tokyo, 7-3-1 Hongo, Bunkyo, Tokyo 113-0033, Japan.
[26] INAF-Osservatorio Astronomico di Padova, Vicolo dell'Osservatorio 5, Padova I-35122, Italy.
[27] Dominion Astrophysical Observatory, Herzberg Institute of Astrophysics, National Research Council of Canada, 5071 West Saanich Road, Victoria, BC V9E 2E7, Canada.
[28] Institute of Astronomy, Madingley Road, Cambridge CB3 0HA, UK.
[29] Institute for Astronomy, University of Hawaii, 2680 Woodlawn Drive, Honolulu, HI 96822, USA.

pact elliptical galaxies and ultra-compact dwarf galaxies (UCDs).

The ACS Coma Cluster Treasury survey was initiated in the fifteenth HST observing cycle following the success of the ACS cluster surveys performed in Virgo (Côté et al. 2004) and Fornax (Jordán et al. 2007). In contrast to the Virgo and Fornax surveys that targeted early-type galaxies, the Coma fields were arranged to maximize spatial coverage at the cluster core in addition to targeted observations in an off-center region of Coma. The advantage of this observing strategy is that it allows for *statistical* measurements of faint cluster members (e.g. the luminosity function) while also probing the effects of the cluster environment across a wide range of cluster-centric distance. Although the Coma cluster is located at a distance of 100 Mpc (5x more distant than Virgo and Fornax), the physical resolution afforded by ACS is similar to current ground-based observations of Virgo and Fornax (∼50 pc).

The ACS Coma Cluster Treasury survey was awarded 164 orbits (82 fields), although the survey was only 28% complete when interrupted by the ACS failure in early 2007. A description of the observing program and image reductions is provided in Paper I (Carter et al. 2008). In this paper, the second in the series, we present source catalogs for the ACS observations completed thus far. The paper is organized as follows: imaging data and calibrations in §2, the methodology for creating source catalogs in §3, a treatment of bright galaxies in §4, and simulations to estimate the completeness and photometric accuracy of the source catalogs in §5.

2. DATA

We refer the reader to Paper I (Carter et al. 2008) for a complete description of the observing strategy and the image pipeline of the HST-ACS Coma Cluster Treasury Survey. Here we provide only a brief summary of the ACS observations and reductions. ACS observations were performed in the F814W and F475W passbands, covering 25 fields located within the virial radius of the Coma cluster (r_{vir}=2.9 Mpc; Łokas & Mamon 2003). The ACS observing footprint is shown relative to the Coma cluster in Figure 2. The majority of the observed fields (19/25) are located at the center of Coma, with six additional fields in the south-west region of the cluster; these regions are commonly referred to as 'Coma-1' and 'Coma-3', respectively (Komiyama et al. 2002).

Processed images and source catalogs for the ACS Coma Cluster Treasury program were released in August 2008 (Data Release 1) [a]. This paper describes the images and source catalogs provided in the second version of the data release, which includes several improvements to the initial release such as: (a) improving the relative alignment between F814W and F475W images, (b) refining the image astrometry, (c) subtracting bright galaxies to improve the detection and photometry of faint neighbors, and (d) improving photometry for very low surface brightness objects (VLSBs).

2.1. *Drizzled Images*

[a] Available from MAST (archdev.stsci.edu/prepds/coma/) and Astro-WISE (http://www.astro-wise.org/projects/COMALS/).

The nominal observing sequence for each field consists of four dither positions ('DITHER-LINE' pattern type) each having an exposure time of 350 s and 640 s for the F814W and F475W filters, respectively. Four fields have only 2-3 dither positions due to the failure of the ACS instrument while the sequence was partially complete. In Table 1 we list the details for each field including a unique identifier taken as the HST visit number, RA/Dec, image orientation, number of dithers, and the integrated exposure time.

Final images were constructed by combining the dither positions with the MultiDrizzle software (Koekemoer et al. 2002). The dithered exposures were individually dark- and bias-subtracted, and flat-fielded through the standard HST-CALACS pipeline software prior to running MultiDrizzle. The steps in the MultiDrizzle process include (a) identifying cosmic rays using a median filter and 'cleaning', (b) aligning the dithered exposures, (c) weighting pixels from the individual dithers by the inverse variance of the background/instrumental noise, and (d) mapping the weighted exposures to an output grid with a pixel size of $0''.05$ pixel^{-1} (*pixfrac*=0.8 and *scale* = 1.0).

A slight spatial offset between F475W and F814W images (∼0.3 pixels) was discovered soon after the initial data release. This offset has a non-negligible effect on the aperture-matched color measurements of condensed objects, such as globular clusters and UCDs, as 0.3 pixels corresponds to ∼7 pc at the distance of Coma. Images were re-aligned by measuring the residual shift between F475W and F814W frames using condensed sources as a reference, and then re-drizzling the F745W band to match the original F814W image. For three fields (visits 3, 10, and 59), it was necessary to re-drizzle the images in both filters to a common pixel position. In Figure 3 we show the spatial offsets between F475W and F814W images after performing the re-alignment procedure. The images, which are part of the version2 data release, are now aligned to within ∼0.05 pixels along each axis.

2.2. *Astrometry*

A two-step process was used to calculate the astrometry for each ACS image, starting with the solution calculated by MultiDrizzle and then performing a fine adjustment using the SCAMP software (Bertin 2006). The initial spatial registration of images from MultiDrizzle was calculated based on reference stars in the HST Guide Star Catalog, although few reference stars are located in the Coma fields owing to its high Galactic latitude (b∼0.88 deg). As a result, the astrometry solutions from MultiDrizzle were accurate to only 1-2″.

Second pass solutions for the ACS astrometry were performed using SCAMP with the goal of aligning images to the SDSS coordinate system. Stars and galaxies from SDSS DR5 were selected as reference objects, which increased the ACS and SDSS matched sample to 18-36 objects for each field. ACS objects with a signal-to-noise ratio less than 3 were excluded from this analysis, as well as objects that were blended with neighbors or located in regions of the image with reduced exposure. Astrometry solutions were calculated for each field using a range of values for the SCAMP input parameters `CROSSID_RADIUS`, `ASTRCLIP_NSIGMA`, and `FWHM_THRESHOLDS`. Note that we forced SCAMP to solve the ACS astrometry *without* using higher order distortion terms (DISTORT_DEGREES = 1) as these values are well constrained by the HST-ACS pipeline (Meurer et al. 2003). We chose the SCAMP configuration that gave the 'best' reduced chi-squared fit (between $0.9 \lesssim \chi^2 \lesssim 1.2$) and the smallest final offset between ACS and SDSS reference objects. This procedure was performed in the F814W waveband and the final astrometry solutions were applied to F475W images.

In Figure 4 we show the average offset in right ascension and declination for ACS/SDSS objects both before and after using SCAMP. The diagram shows that the final astrometry solutions for ACS are statistically consistent with the SDSS system. The rms spread is 0.1-0.2$''$ for each coordinate, which is consistent with the precision of SDSS astrometry (Pier et al. 2003).

The SCAMP solutions for version 1 images were also solved by ignoring higher-order distortion terms, via setting SOLVE_ASTROM = 'N', although this method fixes the location of the WCS reference pixel (CRPIX). By allowing SCAMP to vary the reference pixel location, via setting DISTORT_DEGREES =1, we were able to improve the alignment of the ACS/SDSS coordinates by a factor of ∼5 compared to images released in version 1.

2.3. *Noise Maps*

Noise maps were created for each image in order to improve object detection and to estimate photometric errors. The noise maps were constructed from the inverse-variance images produced by MultiDrizzle, which are stored in the [WHT] extension of the fits images. The WHT images give the background and instrumental noise for the final drizzled images, including the uncertainties related to the flat-field, dark current, read noise, and varying effective exposure across the image (see Paper I).

When estimating photometric errors over large regions (i.e. length scales larger than a few pixels), it is necessary to correct for correlated noise in the drizzled image (Fruchter & Hook 2002). Noise is correlated over small length scales in the drizzled images due to neighboring pixels on the output grid that have flux contributions from the same physical pixel. The net effect of correlated noise is to reduce the single-pixel rms compared to the input image. In contrast, large-scale regions of the drizzled image are relatively free from correlated noise due to a small contribution of any single physical pixel to the total area. As such, photometric errors are underestimated when adding single-pixel noise in quadrature. It has been shown that we can apply a scaling factor to the WHT map to recover its uncorrelated value over large length scales (e.g. Casertano et al. 2000). The corrected noise map, or RMS map, is given by:

$$RMS = \frac{1}{\sqrt{WHT * f}}, \quad (1)$$

where f is the scalar correction for correlated noise, also referred to as the 'variance reduction factor', or by squaring its inverse, the 'noise correlation ratio'.

We have measured the correction factor (f) using a custom autocorrelation script. Specifically, we select a relatively empty 512x512 pixel region within an image, then the script: (a) normalizes the pixels by the effective exposure time, (b) applies a median filter to identify and mask real objects, then estimates and subtracts the background, (c) calculates the autocorrelation function, and (d) measures the correction factor from the autocorrelation image (f=peak/sum). We have measured the correction factor for a subset of images in both filters, recovering an average value of f=0.77. The average value is applied to all WHT maps as the correction factor should depend primarily on the choice of MultiDrizzle parameters *pixfrac* and *scale* (which are constants in our image pipeline).

2.4. *Flag Maps*

The effective exposure time varies abruptly across each image owing to regions that are only partially covered by the dither pattern. These regions are typically located near the image edge or within the ACS chip gap that stretches horizontally across every image. ●Give the typical (fractional) area associated with low exposure regions. Flag maps were created for each image in order to identify pixels with relatively low effective exposure, and we have added additional flags for pixels in close proximity to the image edge and for pixels that are affected by very bright galaxies (§4). The flag values that were assigned to each pixel indicate the following: [0] nominal exposure time, [1] associated with a bright galaxy, [2] located within 32 pixels of the image edge, [4] an effective exposure time less than 2/3 the total integration time, and [8] zero effective exposure.

The main purpose of the flag maps is to identify large regions of each image with similar completeness limits. We note that cosmic rays cleaned by MultiDrizzle often leave a few pixels with low effective exposure, but have little impact on the ability to detect underlying sources. To avoid flagging these pixels as low exposure regions, we applied a 7-pixel median filter to the effective exposure map prior to imposing the low-exposure criteria. A few heavily-cleaned cosmic ray regions remain flagged in each map, which is OK since these objects likely influence source detection.

3. SOURCE CATALOGS

The version 2 source catalogs were created using the SExtractor software (version 2.5; Bertin & Arnouts 1996). SExtractor was chosen because it has become the *de facto* standard for source detection and photometry, and because it offers several features that suit our survey. For instance, SExtractor allows for a separate image to be used for source detection, deblending, and aperture definition, and another image for photometric measurements (referred to as 'dual-image mode'). In addition, SExtractor incorporates the use of RMS maps for source detection and error analysis, as well as flag maps for identifying sources located in select regions of an image.

We elected to run SExtractor in dual image mode using the F814W band as the detection image for both filters. Source detection with SExtractor is performed using a 'connected pixel' algorithm, i.e. a detection is registered when a specified number of contiguous pixels satisfies the detection threshold. We convolved the detection image with a gaussian filter (FWHM=2.5 pixels) to smooth the background noise in order to limit the number of spurious detections due to random noise. The detection threshold for each pixel was set to a constant factor above the sky noise level which is taken directly from the RMS maps described in §2.3. SExtractor parameters for the minimum number of connected pixels (`DETECT_MINAREA` = 5) and the detection threshold (`DETECT_THRESH` = 0.9) were chosen after testing a wide range of values and verifying that obvious sources were detected while minimizing the number of spurious detections. Note that the `DETECT_THRESH` parameter relates to the convolved image, and corresponds to a true signal-to-noise threshold of ∼3. Finally, sources were cross-referenced with the flag maps described in §2.4 and bitwise OR'd across pixels that satisfy the detection threshold. The total flag values are given by the `IMAFLAGS_ISO` field in the source catalogs, and the total number of flagged pixels is given by `NIMAFLAGS_ISO`.

SExtractor performs a second pass analysis of source detections to identify and separate multiple objects that are connected on the sky. This deblending algorithm separates objects using a multi-threshold isophotal analysis that essentially identifies saddle points in the light profile. The wrong choice of SExtractor deblending parameters may result in the inability to separate nearby objects, or in the opposite sense, may produce excessive 'galaxy shredding', i.e. a single galaxy is interpreted as two or more separate objects. The deblending algorithm tends to shred galaxies with significant substructure, thus we chose the F814W band for detection as galaxies are relatively less 'clumpy' compared to the F475W band. We chose deblending values of `DEBLEND_MINCONT` = 0.03 and `DEBLEND_NTHRESH` = 32 to match values used in previous HST studies (e.g. Casertano et al. 2000). These deblending values yield nearly the same number of false blends as false deblends (Benítez et al. 2004). Maintaining a balance between the number of false sources is essential to recovering the true number counts.

SExtractor photometry is performed in the unfiltered measurement image. We performed flux measurements using a variety of apertures defined in the detection image, including isophotal photometry which measures the pixels above the detection threshold (`MAG_ISO`), and adjustable elliptical apertures that are scaled according to the isophotal light profile (`MAG_AUTO` Kron photometry and `MAG_PETRO` Petrosian photometry). We have also performed photometry in a set of nine fixed circular apertures with radii extending between 0.6-6.0″. We adopt Kron magnitudes for this paper which are reported in the instrumental F475W and F814W AB magnitude system. Corrections for Galactic extinction? Photometric errors were estimated by adding in quadrature the background/instrumental errors from the RMS maps described in §2.3 and the Poisson errors from the measured source flux.

3.1. *LSB Galaxies*

Source detection with SExtractor was optimized for bright compact sources as these objects are more numerous across all fields. However, a significant number of extended low surface brightness galaxies (LSBs) are found in the pipeline images. The majority of LSB galaxies are members of the cluster, as such galaxies are common in the central fields, but rare in the outer fields. A fraction of the LSB galaxies were deblended by SExtractor into several smaller pieces, or were simply not detected. We have selected a new set of detection parameters to improve the detection for the subset of LSB galaxies with poor measurements. Sources that were originally associated with the LSB galaxies were removed from the source catalogs.

Try detect_thresh = 0.6 and detect_minarea=16. Try convolving image with a top-hat filter or gaussian with a size characteristic of Coma member (i.e. ∼10″).

3.2. *Spurious Detections*

Constraining the number of spurious detections that contaminate our source catalogs will help to establish useful completeness limits and provide information necessary for statistical studies. In the following sections we have estimated the number of spurious detections in our source catalogs due to cosmic rays and the chance alignment of noise.

3.2.1. *Cosmic Rays*

The majority of cosmic rays were removed using the MultiDrizzle software prior to assembling the final images (Paper I). We expect that a residual number of cosmic rays remain, primarily due to less efficient cosmic-ray removal for fields that have less than four dither positions (e.g. visits 3,12,13,14) or within in regions of every image that are not fully covered by the dither sequence.

Cosmic rays typically appear as bright condensed objects that are detected in a single filter. As such, it is possible to use photometric and structural parameters in the source catalogs to identity cosmic ray candidates. After thorough testing on a sample image, we found that cosmic rays can be efficiently identified by selecting objects with very red colors (`MAG_ISO` colors redder than $F475W$-$F814W$=3) and characteristic sizes smaller than the typical ACS point-spread function (`FWHM_IMAGE` < 2.4 pixels). We limited the identification of cosmic rays to objects in the F814W images that are brighter than I_c=26.5 mag (`MAG_AUTO`), as we are interested in constraining the number of cosmic rays in the detection band up to the completeness limit.

We identified between 18-619 cosmic ray candidates in the ACS fields. The large range reflects... (any ideas? Note that fields with fewer than 4 dithers resulted in both the lowest and highest number of CR detections). The majority of cosmic ray candidates are located in regions not covered by the dither pattern (give percentage). We inspected the cosmic rays candidates in the final images and identified between 2-10 (replace with final value) real objects across each field. The majority of the misclassified cosmic rays are stars, and we removed these objects from the list of cosmic ray candidates. The remaining cosmic ray candidates are flagged in the source catalogs (`FLAGS_CR` = 1). In Table 2 we list the total number of cosmic rays identified in each field (Col [2]), the fraction of detections that are cosmic rays in low-exposure regions (Column [3]), and the fraction of detections that are cosmic rays in regions with nominal exposure time (Column [4]).

3.2.2. *Random Noise*

Spurious detections that result from a chance alignment of random noise fluctuations will dominate the number counts near the completeness limit. It is not trivial to differentiate between noise and real objects from a simple visual inspection of the images and/or selecting candidates using photometric and structural properties (as we did for cosmic rays). Instead, we utilize the fact that there exists an equal number of chance noise alignments that are biased low and high. Specifically, the number of spurious detections due to random noise was estimated for each field by (a) masking known objects, (b) subtracting the background, (c) inverting the image (i.e. changing the sign of all pixels), (d) adding the background to the inverted image, and (e) running SExtractor with the same parameters used to generate source catalogs. This method isolates detections due to random noise and allowed us to measure their of spurious sources across magnitude bins. In Table 2 we list the magnitudes associated with a random noise fraction of 5, 10, 25, and 50% of the total number of detections; the fractions are given for each field and are separated for regions with less than nominal overlap of the dither positions (Columns ●) and for maximum coverage (Columns ●).

4. BRIGHT GALAXY SUBTRACTION – ●GIJS

Bright galaxies have been subtracted from ACS images in order to improve object detection and photometry for faint underlying sources (e.g. dwarf galaxies, GCs). The candidates for galaxy subtraction include 26 Coma members brighter than m_{F814W}=16.7 that are located in 13 ACS fields. Basic properties of the bright galaxy sample are listed in Table 3.

5. SIMULATIONS – ●CARLOS/MARC

Both the detection efficiency and the photometric errors reported in the catalog were determined from simulations consisting of injecting synthetic sources onto the real images, and running the entire detection process through them. Early iterations of the modeling process were also used to fine-tune the SExtractor detection parameters.

For the simulations, the GALFIT code (REF) was used to generate synthetic Sérsic models of given magnitude, effective radius, Sérsic index, ellipticity and position angle. Models uniformly sampled the parameter space shown in Table 1 ●Check; was it logarithmic in Reff?. Indeed, this was a pure detection efficiency experiment, and no attempt was made at this stage to mimic the size-magnitude-concentration distribution of real galaxies. We did not want the simulations to curtail the range of possible solutions; and, besides, the size-magnitude distribution at Coma is complex given the large numbers of background galaxies expected in the images. Nearly 200,000 models were run for each band (Col. 8 of Table 1). Each model was convolved with a TinyTim PSF truncated to 63×63 pixels to increase execution speed, and Poissonian noise was added to match the noise characteristics of the data. The model was finally added at a random position in an HST/ACS frame. Visits 1, 15 (core region), and 78 and 90 (outskirts) were used. SExtractor was then run on the target images using an identical configuration to that used with the real data. Sources were deemed detected if SExtractor detected a source within 4 pixels (roughly 2 PSF FWHM) of the position where a source had been injected.

5.1. *Detection efficiency*

We start by presenting the results on detection efficiency, defined as the probability that a source with given parameters is detected by SExtractor. The efficiency is simply computed as the ratio of the number of detected to injected sources in a given bin of magnitude, size, Sérsic index and ellipticity. It is well known that detection efficiency depends on size as well as magnitude (**???**), and we reproduce that result here. Figure 1 shows efficiency vs. input magnitude for 6 logarithmically-spaced $R_{\rm eff}$ bins from 0.5 to 60 pixels, for four ranges in Sérsic index and ellipticity. The four left and four right panels correspond to $I814W$ and $F475W$ efficiencies, respectively. In all cases, the left-most curve traces the largest $R_{\rm eff}$. All efficiency curves show the same pattern: at the bright end efficiencies are near 100%, and then drop rather abruptly to zero; none of the curves really reaches 100% efficiency, but stays at about 96 to 98%, as a result of sources lost due to being injected near bright galaxies. We list the 80% detection efficiencies in Table 2. Columns (2) to (7) give the F814W efficiencies of each of the six size bins, denoted by $\log(R_{\rm eff})$ in arcseconds; PS stands for point source; columns (8) to (13) provide the corresponding efficiencies for F475W. The table shows that the point-source 80% detection efficiency of the survey is 26.8 I-magnitudes, and 27.8 B-magnitudes.

Efficiencies dramatically drop for more extended sources. Indeed, visual inspection of the SExtractor aperture maps shows a few moderately bright sources that however have not been picked up by SExtractor due to being exceedingly extended. For a given magnitude-size combination, high-$n_{\rm Ser}$ and high ellipticities favor detection, as expected from their enhanced surface brightness when compared with low-$n_{\rm Ser}$ and low-ellipticity sources. We will see in Section **??** that the enhanced detection efficiencies of high-$n_{\rm Ser}$ sources comes with a degraded photometric accuracy.

5.2. *Photometric errors*

6. NUMBER COUNTS – ●DEREK

7. SUMMARY

TABLE 1
REGION OF PARAMETER SPACE EXPLORED BY THE GALFIT- SEXTRACTOR SIMULATIONS.

Band. (1)	Mag. (2)	$n_{\rm Ser}$ (3)	$R_{\rm eff}$ (pix) (4)	Ellip. (5)	Pos. Angle. (6)	# Simulations. (7)
I814W	$20 \rightarrow 29$	$0.8 \rightarrow 4.2$	$0.5 \rightarrow 60.0$	$0.0 \rightarrow 0.8$	$0.0 \rightarrow 360$	180675
B475W	$21 \rightarrow 30$	$0.8 \rightarrow 4.2$	$0.5 \rightarrow 60.0$	$0.0 \rightarrow 0.8$	$0.0 \rightarrow 360$	161667

TABLE 2
80% DETECTION EFFICIENCIES FOR EACH OF THE$R_{\rm eff}$ BINS SHOWN IN FIG. 1.

		F814W						F475W				
Type	PS	-1.08	-0.74	-0.39	-0.05	0.30	PS	-1.08	-0.74	-0.39	-0.05	0.30
(1)	(2)	(3)	(4)	(5)	(6)	(7)	(8)	(9)	(10)	(11)	(12)	(13)
FC	26.8	26.5	26.0	24.9	23.5	21.5	27.8	27.5	27.0	25.5	24.5	22.0
FE	26.8	26.75	26.0	25.25	24.0	22.0	27.8	27.5	27.0	26.0	25.0	23.0
PC	26.8	26.75	26.25	25.5	24.5	23.0	27.8	27.5	27.0	26.3	25.5	23.9
PE	26.8	26.8	26.1	25.5	24.7	23.5	27.8	27.7	27.2	26.5	25.5	24.5

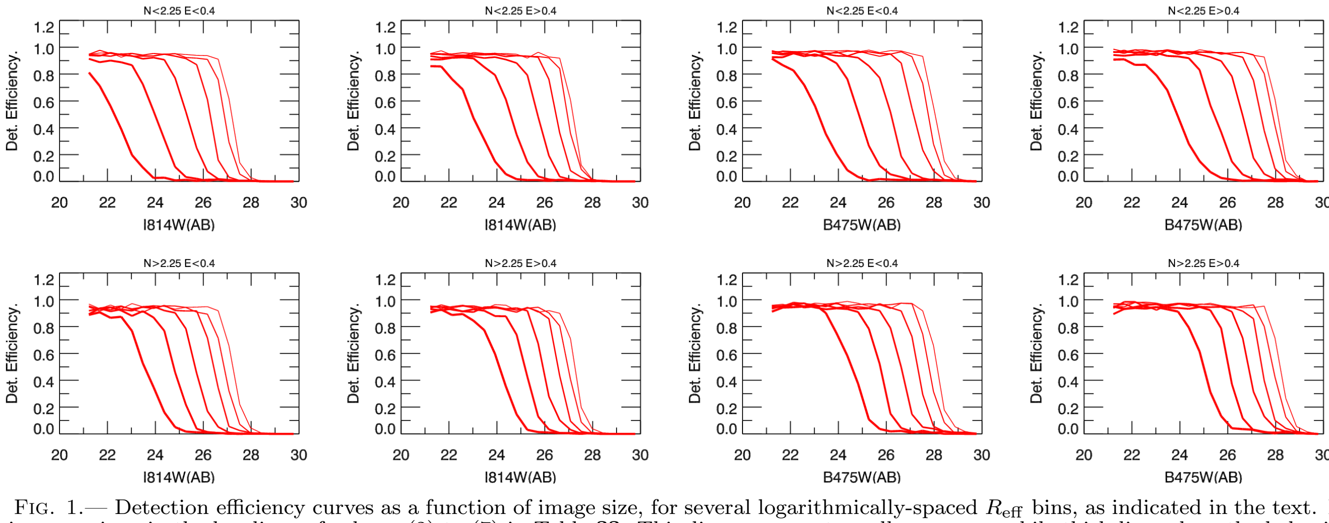

FIG. 1.— Detection efficiency curves as a function of image size, for several logarithmically-spaced $R_{\rm eff}$ bins, as indicated in the text. Bin sizes are given in the headings of colums (2) to (7) in Table **??**. Thin lines represent smaller sources, while thick lines show the behaviour of the sources of increasingly large $R_{\rm eff}$. *Four left panels*: efficiencies for F814W images. *Four right panels*: efficiencies for F475W images.

REFERENCES

Benítez, N., et al. 2004, ApJS, 150, 1
Bertin, E. 2006, in Astronomical Society of the Pacific Conference Series, Vol. 351, Astronomical Data Analysis Software and Systems XV, ed. C. Gabriel, C. Arviset, D. Ponz, & S. Enrique, 112
Bertin, E., & Arnouts, S. 1996, A&AS, 117, 393
Carter et al., A. E. 2008, ApJ, *submitted*
Casertano, S., et al. 2000, AJ, 120, 2747
Côté, P., et al. 2004, ApJS, 153, 223
Ford, H. C., et al. 1998, in Society of Photo-Optical Instrumentation Engineers (SPIE) Conference Series, Vol. 3356, Society of Photo-Optical Instrumentation Engineers (SPIE) Conference Series, ed. P. Y. Bely & J. B. Breckinridge, 234
Fruchter, A. S., & Hook, R. N. 2002, PASP, 114, 144
Jordán, A., et al. 2007, ApJS, 169, 213
Koekemoer, A. M., Fruchter, A. S., Hook, R. N., & Hack, W. 2002, in The 2002 HST Calibration Workshop : Hubble after the Installation of the ACS and the NICMOS Cooling System, ed. S. Arribas, A. Koekemoer, & B. Whitmore, 337
Komiyama, Y., et al. 2002, ApJS, 138, 265
Łokas, E. L., & Mamon, G. A. 2003, MNRAS, 343, 401
Meurer, G. R., et al. 2003, in Society of Photo-Optical Instrumentation Engineers (SPIE) Conference Series, Vol. 4854, Society of Photo-Optical Instrumentation Engineers (SPIE) Conference Series, ed. J. C. Blades & O. H. W. Siegmund, 507
Pier, J. R., Munn, J. A., Hindsley, R. B., Hennessy, G. S., Kent, S. M., Lupton, R. H., & Ivezić, Ž. 2003, AJ, 125, 1559

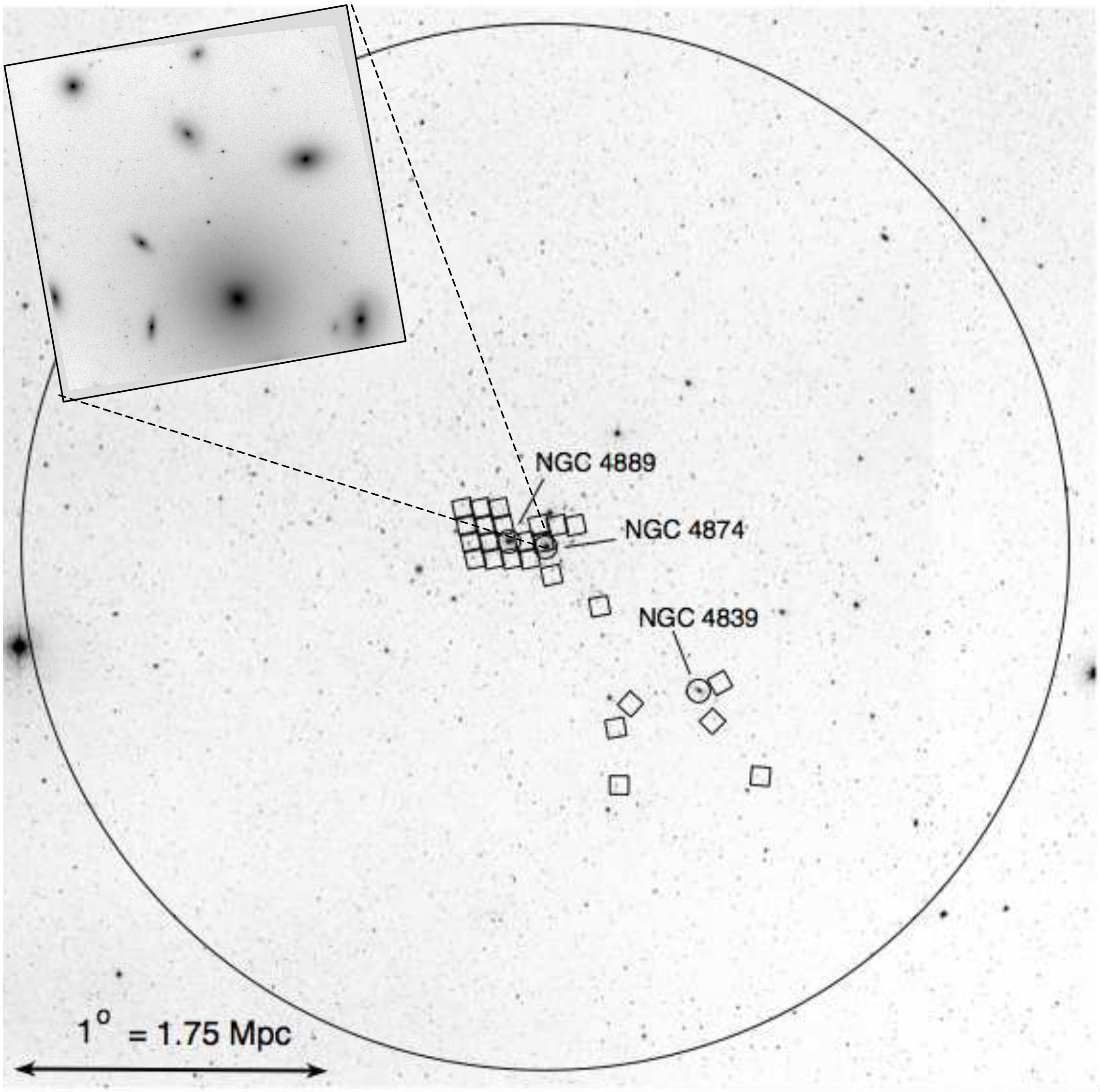

FIG. 2.— DSS image of the Coma cluster showing the location of 25 *HST*-ACS fields observed for the ACS Coma Treasury survey (small boxes). The large circle traces the projected virial radius of the Coma cluster (r_{vir}=2.9 Mpc; Łokas & Mamon 2003). The location of the three cD galaxies in the Coma cluster are indicated by small circles (NGC 4889, 4874, 4839). The inset shows the ACS image for visit-19 ($3.5'$x$3.5'$), which includes the cD galaxy NGC 4874.

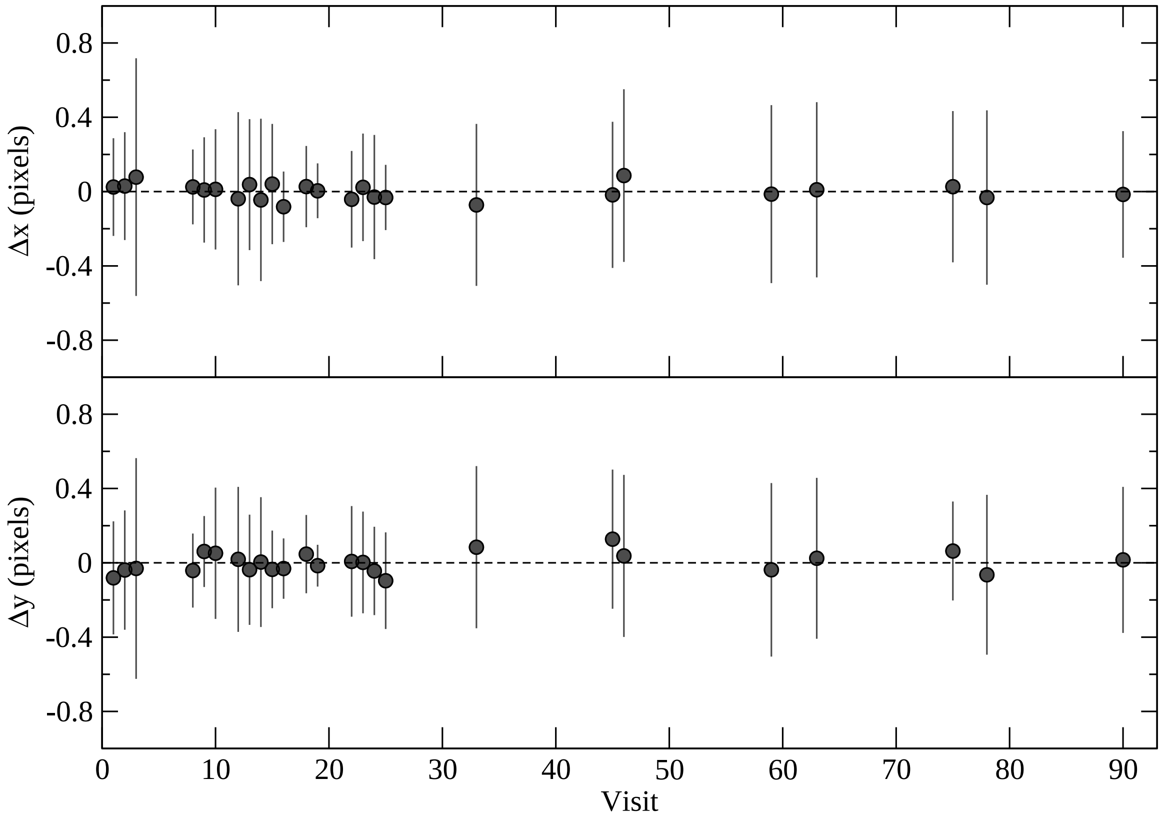

FIG. 3.— The spatial offset for identical objects detected in the F475W and F814W images. Sources were identified using a 5-pixel matching radius giving 300-2000 objects for each field. The 3-σ clipped average offset and standard deviation are shown separately for each visit. The average offset is $\sim$0.05 pixels over both axes, which is a factor of 6 improvement over ACS images provided in the initial data release.

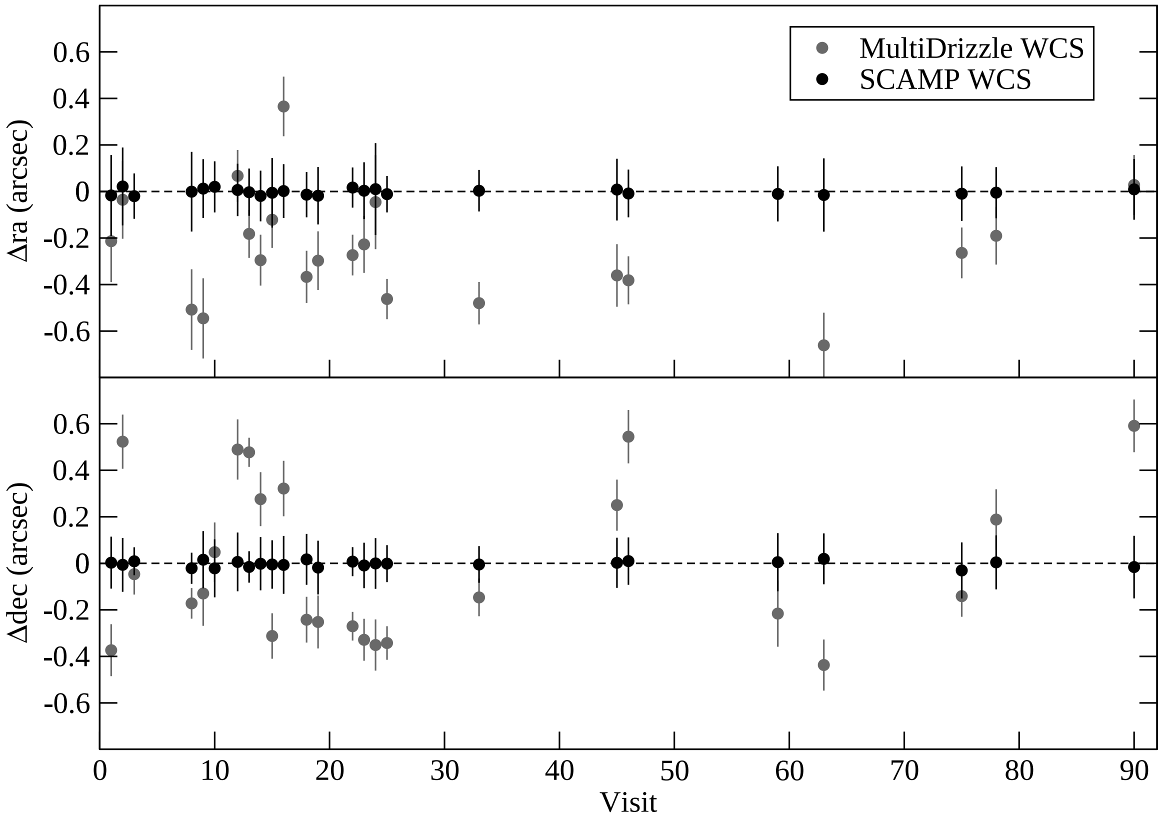

FIG. 4.— The offset in R.A. (top) and declination (bottom) for identical sources detected in ACS and SDSS images. The 3-σ clipped average and standard deviation are plotted separately for each visit. The comparison was performed both before (gray circles) and after (black circles) the SCAMP software was used to align ACS images with the SDSS system. The ACS images are aligned with the SDSS system to within $0''.02$ across each coordinate.

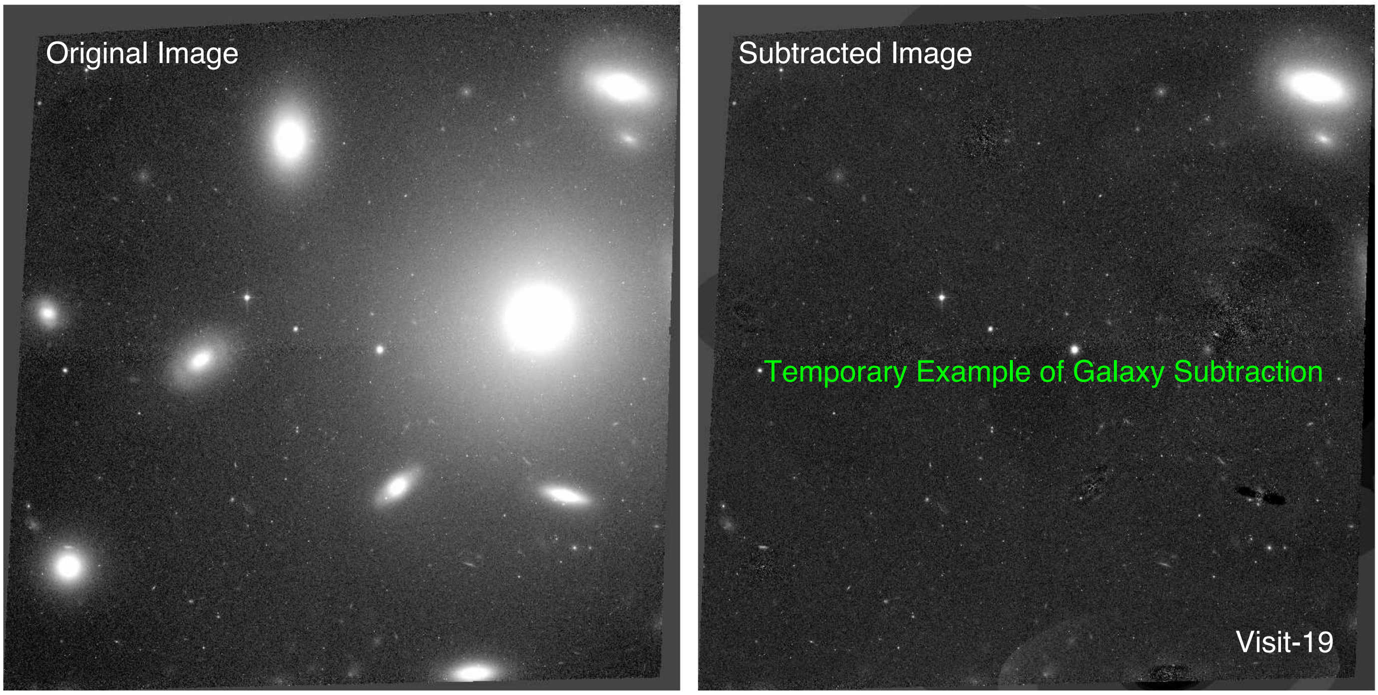

FIG. 5.— A comparison of the original image (left) and galaxy-subtracted image (right) for Visit-19 in the F814W passband. Galaxy subtraction was performed by modeling the light profile using ●. The subtracted image will improve the detection and photometric accuracy of objects located inside the subtracted regions.

TABLE 1
FIELDS OBSERVED FOR THE HST-ACS COMA TREASURY PROGRAM

Field	R.A.	Dec	Orient	Dither	Exposure (sec)	
(visit no.)	(J2000)	(J2000)	(deg)	Positions	F814W	F475W
(1)	(2)	(3)	(4)	(5)	(6)	(7)
01	13 00 45.90	28 04 54.0	282	4	1400	2677
02	13 00 30.30	28 04 54.0	282	4	1400	2677
03	13 00 14.70	28 04 54.0	282	2	700	1397
08	13 00 42.30	28 01 43.0	282	4	1400	2677
09	13 00 26.70	28 01 43.0	282	4	1400	2677
10	13 00 11.10	28 01 43.0	282	4	1400	2677
12	12 59 39.90	28 01 43.0	282	3	1050	2012
13	12 59 24.30	28 01 43.0	282	2	700	1372
14	12 59 08.70	28 01 43.0	282	3	1050	2037
15	13 00 38.70	27 58 32.0	282	4	1400	2677
16	13 00 23.10	27 58 32.0	282	4	1400	2677
18	12 59 51.90	27 58 32.0	282	4	1400	2677
19	12 59 36.30	27 58 32.0	282	4	1400	2677
22	13 00 35.10	27 55 21.0	282	4	1400	2560
23	13 00 19.50	27 55 21.0	282	4	1400	2677
24	13 00 03.90	27 55 21.0	282	4	1400	2560
25	12 59 48.30	27 55 21.0	282	4	1400	2560
33	12 59 29.10	27 52 10.0	282	4	1400	2677
45	12 58 21.58	27 27 40.7	318	4	1400	2677
46	12 58 34.00	27 22 58.8	280	4	1400	2677
59	12 58 31.15	27 11 58.5	270.05	4	1400	2677
63	12 56 29.80	27 13 32.8	265	4	1400	2512
75	12 58 47.75	27 46 12.7	280	4	1400	2677
78	12 57 10.80	27 24 18.0	314.52	4	1400	2677
90	12 57 04.22	27 31 34.5	299.10	4	1400	2677

TABLE 2
Spurious Detections in the SExtractor Source Catalogs

	Cosmic Rays			Random Noise							
Field	Total	Low Exp	Max Exp	Low Exposure (mag)				Max Exposure (mag)			
(visit no.)	CRs	(fraction)	(fraction)	5%	10%	25%	50%	5%	10%	25%	50%
(1)	(2)	(3)	(4)	(5)	(6)	(7)	(8)	(9)	(10)	(11)	(12)
01	49	0.14	0.00								
02	114	0.24	0.01								
03	56	0.08	0.01								
08	112	0.18	0.01								
09	105	0.21	0.01								
10	173	0.29	0.00								
12	619	0.46	0.06								
13	46	0.01	0.01								
14	18	0.06	0.00								
15	114	0.25	0.01								
16	150	0.21	0.01								
18	95	0.16	0.00								
19	94	0.12	0.00								
22	98	0.21	0.01								
23	141	0.25	0.01								
24	127	0.22	0.01								
25	88	0.15	0.01								
33	124	0.25	0.01								
45	69	0.19	0.01								
46	115	0.25	0.01								
59	187	0.32	0.01								
63	131	0.25	0.01								
75	116	0.22	0.01								
78	114	0.24	0.01								
90	123	0.25	0.01								

TABLE 3
Bright Galaxies Subtracted from ACS Coma Images

Field (visit no.) (1)	Galaxy Name (GMP ID) (2)	R.A. (J2000) (3)	Dec (J2000) (4)	F814W Magnitude (AB) MAG_AUTO (5)	MAG_ISO (6)	GALPHOT (7)	F475W Magnitude (AB) MAG_AUTO (8)	MAG_ISO (9)	GALPHOT (10)
01	2440	195.20269	28.09076	13.74	13.71	...	15.11	15.08	...
03	2861	195.05360	28.07551	14.80	14.77	...	16.10	16.07	...
08	2417	195.21455	28.04300	13.70	13.66	...	15.08	15.03	...
08	2551	195.16138	28.01451	13.70	13.66	...	15.08	15.03	...
09	2727	195.09232	28.04697	14.55	14.53	...	15.84	15.82	...
10	2839	195.06144	28.04131	14.45	14.42	...	15.75	15.73	...
10	2940	195.02666	28.00441	14.98	15.02	...	16.26	16.31	...
13	3390	194.88106	28.04656	14.55	14.47	...	...	16.95	...
15	2535	195.17022	27.99663	14.56	14.53	...	15.87	15.85	...
15	2516	195.17814	27.97136	14.07	14.03	...	15.42	15.39	...
15	2510	195.17847	27.96305	14.78	14.77	...	16.10	16.08	...
16	2815	195.06884	27.96754	14.68	14.66	...	15.87	15.85	...
16	2654	195.11655	27.95599	14.83	14.81	...	16.14	16.12	...
16	2651	195.11824	27.97237	14.99	14.97	...	16.21	16.22	...
18	3170	194.94490	27.97386	14.51	14.50	...	15.85	15.84	...
19	3367	194.88662	27.98360	14.09	14.08	...	15.41	15.40	...
19	3329	194.89874	27.95927	13.38	13.36	...	14.76	14.74	...
19	3414	194.87482	27.95646	14.15	14.13	...	15.51	15.50	...
19	3213	194.93219	27.99469	14.82	14.79	...	16.14	16.12	...
22	2541	195.16564	27.92396	14.11	14.09	...	15.44	15.42	...
25	3201	194.93502	27.91248	14.10	14.08	...	15.40	15.38	...
25	3222	194.92628	27.92475	14.99	14.96	...	16.28	16.24	...
33	3423	194.87252	27.85014	14.14	14.10	...	15.51	15.48	...
33	3400	194.87844	27.88428	14.03	14.00	...	15.35	15.32	...
45	4206	194.63358	27.45635	14.91	14.89	...	16.19	16.17	...
46	4192	194.63807	27.36438	15.00	15.00	...	16.23	16.24	...
75	3958	194.71707	27.78504	14.39	14.36	...	15.67	15.65	...
78	5038	194.29486	27.40485	14.89	14.88	...	16.10	16.10	...